Biomagnetic sensing

Hans-Joachim Krause[1] and Hui Dong[2, 3]

[1] Forschungszentrum Jülich, Institute of Bioelectronics, Peter Grünberg Institute (PGI-8), 52425 Jülich, Germany (corresponding author h.-j.krause@fz-juelich.de)

[2] State Key Laboratory of Functional Materials for Informatics, Shanghai Institute of Microsystem and Information Technology (SIMIT), Chinese Academy of Sciences (CAS), Shanghai 200050, China

[3] CAS Center for ExcelleNce in Superconducting Electronics (CENSE) , Shanghai 200050, China

Abstract **Bio**magnetic sensing is a particularly valuable measurement technique because it is non-invasive in nature. Moving ions responsible for the electric activity of cells give rise to a magnetic field surrounding the current flow. Biomagnetic measurements denote the purely passive recording of this magnetic field outside the human body. The challenge is to record these extremely small magnetic fields in the presence of magnetic disturbance fields from the environment. Superconducting Quantum Interference Devices (SQUIDs), the most sensitive magnetic field sensors known to date, are used to measure the minute biomagnetic fields originating from the human heart or brain, in conjunction with attenuation of disturbances from the environment by passive shielding and/or active gradiometric suppression. Magnetic resonance imaging (MRI) is a well-established technique based on exposing the subject to a strong magnetic field, thus allowing to non-destructively measure the distribution of hydrogen atoms within the body. Low-field magnetic resonance imaging (LF-MRI) is a novel measurement technique requiring more than thousandfold lower magnetic fields than conventional MRI, thus allowing to perform imaging with much simpler instrumentation in the presence of metals. Recent experiments yielded promising results with respect to distinction of healthy from malignant tissue. Recently, combinatorial devices allowing to simultaneously record biomagnetic signals and perform magnetic resonance imaging of the anatomy of the human body source are developed to facilitate the determination of the biomagnetic sources by solving the three-dimensional magnetic inverse problem.

Keywords: SQUID, Biomagnetism, Magnetocardiography, Magnetoencephalography, Magnetic resonance imaging, Magnetic immunoassay

1 Introduction

Almost two hundred years ago, Oersted discovered that the flow of electrical currents produces a magnetic field that encircles the current. Inside all animate beings and plants, ions move inside and outside of living cells, as well as from cell to cell. These moving charge carriers give rise to a magnetic field inside and in the vicinity of the creatures. Due to the fact that these natural currents in animals and humans are very small, the ensuing magnetic field is extremely weak. In almost all cases, this so-called biomagnetic field is much smaller than the magnetic field from other environmental sources, such as the earth's magnetic field and the field from man-made sources such as power lines, electric appliances and moving steel objects. Therefore, it is indispensable to shield these environmental disturbance fields in order to be able to record minute biomagnetic fields. In many cases the fields are so small that they can hardly be measured even with the most sensitive magnetic field sensors known to date.

The strongest contributions to the magnetic field intrinsically generated by human beings are from the heart, the so-called magnetocardiogram (MCG), from muscles (magnetomyogram), and from the brain, the magnetoencephalogram (MEG). Biomagnetic measurements denote the contact-free registration of this magnetic field emitted from the body of the human or animal subject. This measurement is entirely non-invasive and purely passive. No excitation whatsoever is incident on the subject; just the magnetic field generated by the ongoing electrical action currents are recorded at one or more positions outside the body. Due to the non-magnetic properties of almost all tissue types, the magnetic field is practically unaffected by the intermediate tissue between source current and measurement location. In particular, the varying electrical conductivities of the different types of tissue between source and sensor do not influence the magnetic field, whereas they do influence the voltages during electrocardiogram (ECG) recordings. Therefore, finding a solution to the inverse problem for noninvasive 3D localization of intracardiac sources is much easier when using MCG data as compared to ECG recordings.

2 Superconducting Quantum Interference Devices

A SQUID consists of a superconducting loop with one or two Josephson junctions. It combines the effects of quantization of magnetic flux in units of the magnetic flux quantum $\Phi_0 = 2.07\times10^{-15}$ Vs and the dependence of the supercurrent circulating in the loop on the magnetic flux threading the loop. The SQUID is an extremely sensitive converter of magnetic flux to output voltage. With a feedback electronics that compensates the measured flux with counter-flux to maintain a stable operating point, the device can be used as a linear null detector. SQUIDs are capable of re-

solving better than 10^{-6} of Φ_0, which makes them the most sensitive sensors of magnetic flux known to date. Typical readout electronics offer a frequency range extending from direct current (dc) to MHz with a dynamic range of 120 dB or more. In the case of SQUIDs fabricated from conventional, low-temperature (low-T_c) superconductors, operation is usually done at the boiling temperature of liquid helium (T = 4.2 K) whereas high-temperature superconductor (high-T_c) SQUIDs are used in liquid nitrogen at 77 K. A comprehensive coverage of SQUIDs can be found in Ref. [1].

The most common type of SQUID is the dc SQUID schematically shown in **Fig. 1 a**. It contains two Josephson junctions connected in parallel to a bias current source by a superconducting loop of inductance L_s. The voltage drop across the junctions is measured. When external magnetic flux Φ_e threads the SQUID loop, the ensuing circulating current $I = -\Phi_e/L_s$ in the ring adds to the bias in one junction while subtracting in the other. With increasing Φ_e, junction phases are switching alternately, and the current I is reversing direction at each $\Phi = \Phi_0/2$. Consequently, the current-voltage (I-V) curve measured across the junctions is alternating between two extreme traces: the upper one corresponding to integer flux, $\Phi = n\Phi_0$ (n = 0, 1, 2, 3, ...), and the lower one corresponding to half integer flux, $(n+½)\Phi_0$, as shown in **Fig. 1 b**. The voltage V across a dc SQUID is thus a periodic function of Φ_e with the period of Φ_0, see **c**. The ultimate flux sensitivity is limited by thermal and $1/f$ low-frequency flux noise components which originate in the SQUID itself and in the feedback electronics. Usually, the intrinsic dc SQUID noise is larger than that of the electronics and thus determines the resolution.

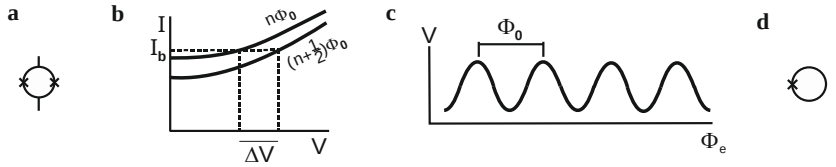

Fig. 1. a dc SQUID, consisting of a superconducting loop with two Josephson junctions marked by crosses, **b** I-V curve for integer and half-integer flux threading the SQUID loop, **c** V-Φ curve, **d** rf SQUID, consisting of a superconducting loop with one Josephson junction.

Another relatively common SQUID type is the radio-frequency (rf) SQUID, schematically shown in **Fig. 1 d**. It contains only one Josephson junction in the loop which is inductively coupled to a resonant LC circuit which applies a rf bias current to the SQUID. Similarly as in case of the dc SQUID, the voltage across the resonant circuit is a periodic function of the magnetic flux threading the loop. At low-T_c, the ultimate sensitivity of dc SQUIDs is better than that of rf SQUIDs. At higher operation temperature, this advantage is less predominant. The advantage of rf SQUIDs over dc SQUIDs is that they do not require galvanic contacts to the sensor, making them safe against static discharge.

SQUIDs are flux sensors of unequaled sensitivity. In most magnetometric applications, however, the task is to measure the local intensity of magnetic field B =

Φ/A, with A denoting the area over which the flux is collected. To measure very small magnetic fields B, the pickup area A needs to be of the order of mm^2 or even cm^2. Hence, SQUID magnetometers must include flux pickup structures having a sufficiently large effective area, A_{eff}. The low-inductance SQUID loop alone has a very small A_{eff} of the order of 10^{-3} mm^2, which is not sufficient in most cases. For low SQUID noise, its inductance L_s should be as small as possible, but for good field sensitivity, a large A_{eff} yields a large L_s. This conflict can be resolved by collecting the magnetic flux Φ over a larger area and coupling it more or less effectively to the very small SQUID hole. The simplest solution is to make the outer dimensions of the SQUID loop much larger than the loop's hole in order to concentrate into that hole a fraction of the flux expelled from the superconductor due to the Meissner effect. This scheme is called washer SQUID. Much higher effective areas A_{eff} can be obtained using flux transformers. They consist of a pick-up coil, a pair of interconnecting leads, and a multiturn input coil inductively coupled to the SQUID, see **Fig. 2 a**. In order not to deteriorate performance by thermal Johnson noise, the whole flux transformer circuit is superconducting.

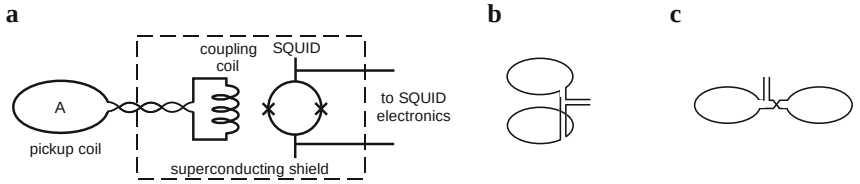

Fig. 2. a Flux transformer, consisting of a pickup coil and a coupling coil made from superconducting wire, inductively coupled to a SQUID, **b** axial gradiometer, consisting of two counter-wound pickup coils above each other, **c** planar gradiometer, with counter-wound pickup coils next to each other.

In biomagnetic applications, very weak signals from localized sources such as heart or brain have to be measured against a background of magnetic disturbances which are orders of magnitude stronger, but more uniformly distributed in space because they stem from far sources, like power lines or cars. In such cases, the use of gradiometers is an alternative to magnetic shielding. For example, in the simplest case of a single first-order gradient component, two coils having identical areas A and a spacing b called baseline, are connected in series-opposite, as shown schematically in **Fig. 2 b** for $\partial B_z/\partial z$ (axial gradiometer) and **Fig. 2 c** for $\partial B_z/\partial x$ (planar gradiometer). Higher-order gradiometers that measure second and higher order spatial gradients of the magnetic field are made similarly using more pickup coils. Planar gradiometers can be fabricated in thin-film technology. However, the axial version involves 3D superconducting wire structures, and thus is feasible only with low-temperature superconductor technology. High-T_c axial gradiometers require the usage of two or more SQUID sensors and electronic subtraction of the SQUID signals.

Low-T_c SQUID sensors are usually fabricated in thin-film niobium technology using magnetron sputtering on oxidized silicon or quartz wafers. The SQUID structure and the junctions are photolithograhically patterned from $Nb/AlO_x/Nb$ trilayers, where the aluminium oxide barrier is formed by thermally oxidizing a nanometer-thin aluminum layer. Additional metallization is used for bonding pads and for fabrication of junction shunts. The insulation between Nb and conducting layers is usually obtained by depositing silicon oxide films and by edge anodization to form an insulating NbO_x oxide. SQUID and input coil of the flux transformer are usually integrated into one monolithic thin-film structure. For biomagnetic applications, the complete magnetometers and gradiometers are often made with 3D Nb-Ti wire-wound pickup coils bonded to Nb pads of the input coil.

High-T_c SQUID sensors are typically fabricated from $YBa_2Cu_3O_{7-x}$ (YBCO) epitaxial thin films deposited on single crystal $SrTiO_3$, MgO or $LaAlO_3$ substrates with surface polished to epitaxial quality. The most popular Josephson junction type is the grain-boundary junction. The grain boundary can for instance be formed by depositing YBCO on a bicrystal substrate assembled from two single crystals which are glued together with twisted crystal orientations. Another approach is to etch a ditch into the substrate and to grow the YBCO film across this so-called step edge. The YBCO SQUID structures are patterned by optical photolithography of films followed by argon ion beam or wet-chemical etching.

3 Biomagnetism

The term “biomagnetism” denotes the measurement of the natural magnetic field generated by a living creature due to the movement of electric charge carriers inside the body [2]. Both intra- and extracellular currents, as well as the exchange of ions between cells contribute to the electrical currents inside the body and thus to the magnetic field surrounding the currents [3]. MCG and MEG are the most common biomagnetic modalities. Other electrically active organs are also known to produce detectable magnetic fields. The field of the eye is called magnetooculogram, the field of the stomach is the magnetogastrogram.

3.1 Magnetocardiography

The heart of mammals, in particular the human heart, consists of heart muscle cells, so-called myocardial fibers, arranged as series of cells connected with intercalated discs. These discs act as connectors that allow the electrical excitation to propagate successively from cell to cell [4]. In order to pump blood through the body, all the muscle cells in the atria and in the ventricles have to be excited quasi simultaneously. This is performed by the natural pacemaker, the so-called sinus node, located close to the entry of the vena cava superior into the right atrium. In ECG as well as

in MCG, sinus node and atrial depolarization are seen as so-called P wave, following the well-known terminology of Einthoven [5] who named the characteristic ECG peaks using the letters P, Q, R, S, and T. Then, the excitation signal reaches the atrioventricular (AV) node which provides a ~120 ms time delay. The excitation is then distributed from the AV node to both ventricles by means of the His bundle and the Purkinje fibers. The depolarization of the ventricles gives rise to the QRS complex of ECG and MCG signal which is the strongest signal of the heart. A typical adult exhibits a peak-to-peak QRS signal of ~100 pT directly above the chest, see **Fig. 3**. Electrical excitation leads to synchronous depolarization of the heart muscle cells. After about 200 ms of refractory period, the heart muscle cells repolarize, leading to the characteristic broad T wave in the signal.

The electrical activity of the human heart by measuring the voltage on the skin of the patient was already measured in the late 19th century. In the early 1900s, ECG was fully established [5]. Because the magnetic field associated with the intracorporal electric current of the heard is so small, it took another 60 years until the first magnetic recording of the human heart was performed by Baule and McFee [6] using induction coils. With the invention of the Superconducting Quantum Interference Device (SQUID) in the 1960s [7], sufficiently sensitive magnetometers became available [8], allowing to record MCG with higher quality [9] and eventually leading to a breakthrough in biomagnetic measurements [10].

The first MCG measurements were performed with just one SQUID channel. Single-channel instruments, however, required tedious sequential recordings at different positions above the patient's chest, thus significantly prolonging the measurement time [11]. Therefore, MCG instrumentation was gradually improved from single channel towards multichannel devices [12]. Multichannel SQUID systems for biomagnetic measurements were developed first at Helsinki University [13]. Subsequently, multichannel systems were developed and commercialized by the companies Neuromag (24 channels in 1989), Siemens (37 channels, 1989), Dornier (28 channels, 1990), Philips (62 channels, 1993), and Elekta (99 channels, 2000) [14]. All these systems rely on liquid helium cooling which constitutes a major cost item in their continuous operation.

Another serious drawback that hampered clinical applications was the requirement for expensive and bulky magnetically shielded rooms to suppress environmental disturbance signals. At Helsinki Hospital, MCG was recorded with a SQUID-based gradiometer in a wooden cottage [15]. MCG systems with 9 or 36 channels for unshielded operation were commercialized by CardioMag Imaging Inc [14].

With the advent of high-T_c superconductors in 1986, SQUIDs made of $YBa_2Cu_3O_{7-x}$ became a promising alternative for biomagnetic measurements. They only require liquid nitrogen as coolant, thus cutting down operating costs to negligible values as compared to helium-cooled systems. However, they do not reach the same sensitivity as their low-T_c counterparts and their production is much less reproducible and reliable. Nevertheless, several high-T_c systems for MCG were realized for shielded [16,17,18] and unshielded operation [19]. The application of the

four-channel system to adult magnetocardiography and to fetal magnetocardiography has been shown in [20]. The system has been utilized for educational purposes in Jülich, measuring the MCG of more than 3000 high-school students.

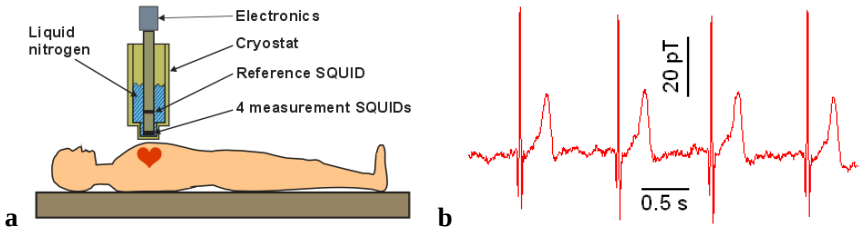

Fig. 3. a Principle of MCG measurement; **b** Typical human MCG measured with high-T_c rf SQUID.

Numerous clinical trials have been performed regarding the application of MCG to different heart problems. Applications include the detection of myocardial ischemia [21] and viability [22], coronary artery disease [23,24,25], arrhythmogenic risk assessment, imaging of arrhythmogenic sites such as the Wolff-Parkinson-White syndrome [26] or ventricular arrhythmia [27].

3.2 Fetal Magnetocardiography

The MCG of an unborn baby in the mother's womb was measured for the first time in 1974 with an unshielded SQUID system [28]. Fetal magnetocardiography (fMCG) is a reliable method for noninvasive study of fetal cardiac electrophysiology from the 20th week of gestation on, especially during the third trimester of pregnancy when the electrically insulating vernix caseosa hampers abdominal recording of fetal ECG [29]. In addition, maternal ECG obscures fetal ECG. Systematic studies on the analysis of cardiac time intervals have been performed in [30]. Other common fetal monitoring techniques such as cardiotocography and echocardiography lack the temporal resolution to extract such information. fMCG has been shown well applicable to the early diagnosis of arrhythmia [31,32]. For the early detection of congenital heart defects, however, only a few fMCG case reports have been reported [29]. Here, echocardiography appears to be the method of choice. Albeit the sensitivity is not as high as in case of usual helium-cooled SQUIDs, it is possible to record fMCG with high-T_c SQUIDs [33], see **Fig. 4**. In order to study the electrophysiology, averaging and subtraction of the maternal MCG is needed, in contrast to low-T_c instrumentation that yields sufficient signal-to-noise even in real time.

Once that instrumentation becomes more robust and can operate outside magnetic shielding, it is expected that fMCG finds widespread acceptance because it is the only modality that allows to study the electrophysiology of the fetal heart.

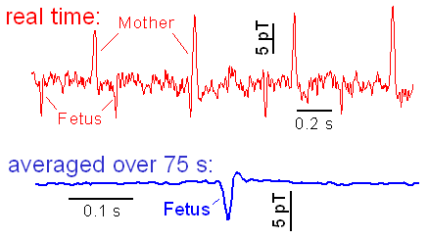

Fig. 4. Typical real-time fetal MCG signal, measured with high-T_c rf SQUID, and fetal signal averaged over 75 s.

3.3 Magnetoencephalography

Measuring the magnetic field of neuronal brain activity with MEG is more challenging than MCG because the magnetic field of the human brain is about hundredfold smaller than that of the heart [34]. The electrical ion currents flowing in the human head tissue give rise to a magnetic field that can be observed outside the skull. The currents include both intracellular "impressed" currents by neural activity, and the so-called "volume current" of freely moving ions in the extracellular space. The latter can be modeled as a conductive medium with an electrical conductivity depending on the type of tissue, i.e. white matter, gray matter etc. The total magnetic field is determined by a summation over all current elements in the whole head according to Biot-Savart's law. To a good approximation, the magnetic field generated by the impressed currents is orthogonal to the scalp surface, whereas the contribution from the volume currents is tangential to it [35]. Thus, the contribution of volume currents can be neglected in the most common measurement configuration that registers just the magnetic field component orthogonal to the scalp. In the case of pyramidal neurons with an open-field structure [2], predominantly consisting of a single dendrite and one long axon, the small current flowing in the dendrite due to membrane depolarization after neurotransmitter intake at the synapse can be modeled as a current dipole with a field $B \propto 1/r^3$, where r denotes the distance. This current dipole contributes to the magnetic field. A typical current dipole of one postsynaptic dendrite has a magnetic moment of 2×10^{-15} Am, which gives rise to a magnetic field contribution of 3×10^{-19} T at a distance of 5 cm [35]. The summation of current dipoles from the pyramidal neurons is orthogonal to the scalp surface and results in a detectable biomagnetic signal. Considering a magnetic field resolution of typical MEG instrumentation of a few fT/√Hz, it becomes obvious that approximately 50,000 synchronously firing neurons are needed to obtain a measureable signal.

The so-called "action potential" (AP) contribution to the brain's magnetic field is obtained from the depolarization current flowing along an axon, followed by a repolarization current restoring the rest state potential. Thus, the AP consists of a pair of current dipoles with opposing directions, a current quadrupole, which yield

a field $B \propto 1/r^4$ that is about tenfold smaller than that of a dipole because it decays more with distance.

Multichannel MEG instrumentation has been developed and commercialized by a number of companies, including the Magnes systems from 4-D Neuroimaging (formerly BTi) with up to 248 channels, the CTF MEG systems from VSM MedTech with up to 275 channels, the Elekta Neuromag systems with up to 306 channels, and the ARGOS systems from Advanced Technologies Biomagnetics with up to 495 channels [14]. In order to accommodate as many SQUIDs as possible as close to the scalp as possible, these systems are equipped with helmet-shaped cryostats. The systems have been designed for everyday clinical use operated by technicians. They include computer-controlled equipment for visual, auditory and tactile stimulation of neuronal activity. Some systems allow to simultaneously record electroencephalograms (EEG).

Detailed studies of the normal function of the primary sensory and motor system were performed, thus establishing a basis to assess dysfunctions later. Techniques to evoke somatosensory activity include electric, tactile and laser stimulation to the skin, preferably of the peripheral nerve at the wrist. It was found that the first cortical component about 20 ms after stimulation (called N20) is completely exogenous and not affected by attention. The functional analysis of the auditory cortex was performed by sine-wave tones of different frequencies and duration and localization of the tonotopic organization of the cortex. Stimulation of the visual system was done by pattern reversal, flashes and moving stimuli. Primary answers as well as entrainment of the alpha rhythm were studied. Examinations of the movement-evoked magnetic field include both self-paced and externally paced movements, preferably of the fingers. Synchronization mechanisms for control of movements were also studied.

A big challenge to MEG and other brain imaging modalities is the identification of higher cognitive functions because neuronal networks exhibit a high spatial and temporal complexity and a great individual variability. The idea is that certain brain regions are responsible for certain tasks.

MEG studies yielded significant contributions to the revelation of brain processes in reception and processing of speech signals. For instance, a specific electrophysiological component has been identified about 150 ms after the onset of a critical word [36]. A second peak named N400 at around 400 ms is correlated to lexical-semantic integration [37]. With respect to the recognition of written language, several relevant areas such as Broca's and Wernicke's area were localized, demonstrating the usefulness of MEG for presurgical planning [38]. By manipulating the expectancy of the final words of a sentence, semantic processing of words on the sentence level during reading was investigated and found to be also related to the N400 peak [39]. Music is perceived differently than speech, albeit there are similarities [40]. Especially the response to harmonic violations are fast and can be localized near the primary auditory cortex [41].

A fundamental question in neuroscience is how the brain groups different sensory inputs such as sound pitch, timbre and volume, color and intensity of light, and

olfactory stimuli, to form recognizable objects. With support from MEG studies, the assumption was made that synchronous oscillations in the so-called γ band at around 40 Hz play a role in the process. A review on this so-called binding process is given in [42]. Nonoscillatory magnetic brain responses have also been studied with respect to feature binding and object recognition [43].

Another important field of brain research involves the study of motor actions. Preparation, control, and execution of movements involve transient, slow, and oscillatory magnetic activity in both primary sensory-motor and higher cognitive areas. The role of the so-called magnetic μ-rhythms for the preparation and execution of movements was investigated by means of event-related spectral power changes [44].

MCG is clinically used for evaluating normal and abnormal brain functions, and for the localization of cortical sources. Currently, the localization of epileptic discharges and presurgical brain mapping represent the most common clinical applications [45,46]. For presurgical evaluation in patients with intractable focal epilepsy, MEG is medically necessary to localize areas of epileptic activity. There is a need to measure small epileptic discharges with bigger background brain activity. Other diagnostic applications remain in the research stage.

Normal spontaneous brain activity of EEG and MEG consists of various frequency bands. Alpha waves (8–13 Hz) are dominant when the subject is awake, beta waves (>13 Hz) are seen during wakefulness and light sleep. Theta (4–7 Hz) and delta (<4 Hz) rhythms are usually observed during sleep, but they may also appear due to brain tumors and ischemia. The source of the spontaneous activity, both normal and abnormal, spreads over the bilateral cerebral cortices, so that separation of each generator is hardly possible with EEG. The higher spatial resolution of MEG may help to localize abnormally slow waves [47,48] due to structural brain lesions. Ischemia of the brain can also be detected with MEG. Stenotic lesions of the internal carotid artery system sometimes yields an oscillatory signal at 6–8 Hz in the temporo-parietal area [49].

It has been successfully shown that MEG is even feasible with high-T_c SQUID instrumentation. By comparison with the result obtained from a commercial 248 channel whole-head MEG system, it was demonstrated that the sources of auditory evoked responses can be localized with similar precision using a single high-T_c dc SQUID magnetometer operating at 77 K [50]. However, a long way of development is still needed until nitrogen-cooled SQUID systems will have matured to be suitable for routine MEG recordings.

Today, there are more than 130 MEG systems installed worldwide, which is a relatively small number as compared to the approximately 36,000 MRI machines. The application of MEG is still mainly focused on research, i.e. all the different aspects of brain activity listed above. Routine clinical applications are still scarce. In order to fully establish MEG in clinical practice, the reliability of source estimation needs improvement. Inversion software should be improved, in particular for multiple source estimation to overcome the nonuniqueness of the electromagnetic

inverse problem. For clinical research, a validation of the source estimation accuracy of MEG by fusion with other imaging modalities is needed. MEG has excellent time resolution but is not perfect with respect to localization accuracy. Therefore, a combination with low field MRI as an anatomical imaging modality becomes particularly promising for future work (see section 5 on hybrid biomagnetism).

4 Magnetic resonance imaging

Magnetic resonance imaging (MRI) is a powerful and probably the most versatile medical imaging modality for the human body [51,52]. This technique is developed from nuclear magnetic resonance (NMR) [53]. The MR signal originates from the nuclei with nonzero spin, and protons are conventionally most-commonly imaged because of widely distribution in human body fluids, proteins, lipids, glucose, etc. In a static magnetic field B_0 along z direction, an energy difference $\Delta E = \gamma\hbar B_0$ occurs dependent on if the spin is aligned parallel or antiparallel to the field, with γ denoting the gyromagnetic ratio (in case of proton: $\gamma/2\pi$ = 42.58 MHz/T) and $\hbar$ being Planck's constant h divided by 2π. The populations of parallel and antiparallel spins are nearly equal. For example, at B_0 = 1 T, the ratio between the two types of spins is approximately 1.000007. The net equilibrium magnetization of the spin system can be expressed as $M_0 = \rho\gamma^2\hbar^2 B_0/(4k_B T)$, in which ρ is the spin density and T the temperature.

The imaging of nuclei is realized by applying linear three-dimensional magnetic field gradients $\boldsymbol{G} \equiv \frac{\partial B_z}{\partial x}\hat{\boldsymbol{x}} + \frac{\partial B_z}{\partial y}\hat{\boldsymbol{y}} + \frac{\partial B_z}{\partial z}\hat{\boldsymbol{z}}$. Each component is generated by special coils and can be controlled separately. The gradients $\boldsymbol{G}$ will encode the precession frequency (or phase) by the spatial position of the proton. By applying specific pulse sequences and a spatial Fourier transform, three-dimensional images can be acquired.

Certain nuclei (commonly hydrogen) can absorb and emit rf energy. The application of an rf pulse causes the protons to precess about B_0 at their Larmor frequency $f_L = (\gamma/2\pi)B_0$. During the precession, M_0 undergoes two relaxation processes. The longitudinal relaxation, characterized by the relaxation time T_1, reflects the interaction between spin and nearby lattice with energy exchange which causes the longitudinal magnetization back to equilibrium. The transverse relaxation, characterized by the relaxation time T_2, describes the dephasing process of net magnetization in the transverse plane. There is no energy lost in the transverse relaxation process, and $T_2 \leq T_1$. In tissues, T_2 and T_1 are both field-strength dependent, and they may range from tens of milliseconds to about one second. The T_1 (or T_2) weighted MRI images may show the diseased tissues like tumors by different image contrasts because these malignant tissues usually exhibit different relaxation times from the normal tissues.

4.1 High-field MRI

In conventional MRI technique, a Faraday coil oriented perpendicularly to B_0 is used to transfer the precession of magnetization to the voltage output, according to the Faraday's law of electromagnetic induction. The induced electromotive force V is proportional to the rate of change of flux in the detection coil, namely $V \propto \mathrm{d}M/\mathrm{d}t \propto 2\pi f_L B_0 \propto B_0^2$. The signal-to-noise ratio (SNR) is one of the key parameters for MR images. The fact that the signal output is proportional to the square of B_0 resulted in the continuous pursuit of increasing B_0 field strength, from the millitesla to the Tesla range, during MRI history.

The NMR phenomenon was observed independently by Purcell group [54] and Bloch group [55] in 1946. In 1966, Ernst introduced the pulsed Fourier transform into NMR, which pioneered the MRI technique [56]. Seven year later, Paul Lauterbur acquired the first MR image [57]. In 1977, Peter Mansfield proposed the Echo Planar Imaging (EPI) technique which significantly accelerated the scan time and made the real-time clinical scanning become possible [58]. In 1980s, the full-body MRI scanners were developed rapidly and the MRI industry became blooming. MRI produces high-quality images of the human body with good tissue contrast and has proven to be a versatile tool for biological research and medical applications. Nowadays, there are more than 36,000 MRI machines working in hospitals, universities and research institutes for a multitude of medical applications including diagnosing and studying the central nervous system, like brain and spinal cord, joint disease, and organs, like liver and pancreas. Further prominent application examples include functional magnetic resonance imaging (fMRI) [59,60], flow imaging (MRI angiography) [61,62], diffusion-weighted imaging [63,64], and magnetic resonance spectroscopy (MRS) [65]. Besides the most commonly used proton MRI, the X-nuclei MRI, which images different nuclei (e.g. ^{17}O, ^{19}F, ^{23}Na, ^{31}P, ^{35}Cl), may provide complimentary information to proton MRI in physiological processes [66].

fMRI is well suited for brain function analysis. Neural activity causes increased metabolic activity and blood flow in the adjacent vessels to feed the activity. As the metabolic activity takes oxygen from the diamagnetic hemoglobin, the amount of unoxygenated paramagnetic hemoglobin is increased, thus locally affecting the MRI signal [67]. This method called blood oxygen level dependence (BOLD) has various medical applications to identify brain pathologies. The association of neural activity with BOLD has been established recently [68].

4.2 Low-field MRI

At present the typical field strengths of clinical MRI systems are 1.5 and 3.0 Tesla, usually produced by superconducting magnets, resulting in expensive, large and complex systems. In the decades since the discovery of NMR phenomena, people have been working on low-field (LF) NMR and MRI at microtesla range, the same order of magnitude as earth's magnetic field (about 50 μT). Since the B_0 field

strength is reduced by four orders of magnitude, the detection sensitivity of the Faraday coil can no longer meet the requirements of the imaging SNR. In order to increase SNR, there are two common methods. First, SQUIDs are used as detectors instead of Faraday coils. The SQUID with a sensitivity of up to 10^{-15} T/√Hz is one of the most sensitive magnetic field sensors, and its sensitivity is independent of frequency [69]. Alternatively, the introduction of pre-polarization will increase the initial macroscopic magnetization of the sample and finally improve SNR. In this technique, a strong magnetic field pulse *(*B_p*)* is applied to pre-polarize the sample, and then the MRI signal is detected in the B_0 field.

In addition, the entire system can be housed in a magnetically or conductively shielded room. The external magnetic field noise in the signal frequency bandwidth will be attenuated and the SNR can be improved. However, the rapid switch-off of B_p—typically in 10 ms—to avoid significant decay of the magnetization before signal acquisition induces transient eddy currents in nearby conducting objects, most notably the walls of the shielded room, see **Fig. 5**. The resultant inhomogeneous magnetic-field transient may both seriously distort the spin dynamics of the sample and exceed the dynamic range of the SQUID readout electronics, and must be greatly reduced before one can begin image encoding and acquisition.

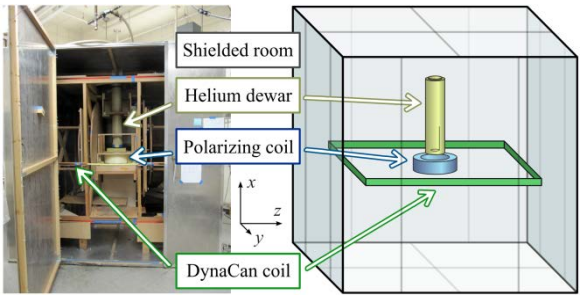

Fig. 5. Aluminium shielded room containing the liquid-helium dewar, the B_p coil and the DynaCan coil.

We developed the so-called dynamical cancellation (DynaCan) technique to suppress adverse, pulse-induced transient eddy currents [70]. DynaCan exploits the fact that eddy currents are typically a superposition of modes that decay exponentially with their individual time constants. Different time constants correspond to different spatial eddy-current patterns. An additionally pulsed magnetic-field waveform with features at corresponding time scales thus allows selective coupling to the dynamics of the individual patterns (**Fig. 6**). This cancellation pulse is provided by a current fed into a separate coil, spatially larger than the B_p coil, during the later part and turn-off of the polarizing pulse. The computationally determined DynaCan current waveform is designed to drive the eddy currents to zero at the precise moment that the polarizing field becomes zero. With DynaCan we demonstrated a reduction of the eddy-current fields by 99% (**Fig. 7**).

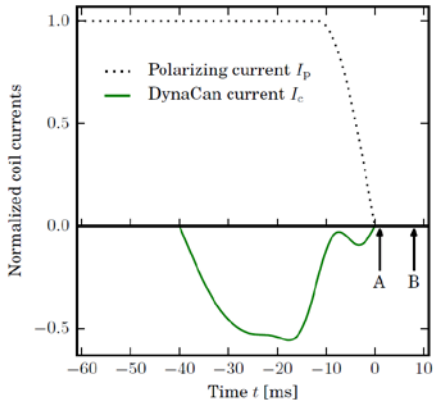

Fig. 6. Dynamical cancellation waveform I_c and end of pre-polarizing pulse I_p; the currents are normalized to the amplitude of I_p. Arrows indicate logic switching instants for (A) opening relays in the B_p and DynaCan coil circuits and (B) beginning data acquisition.

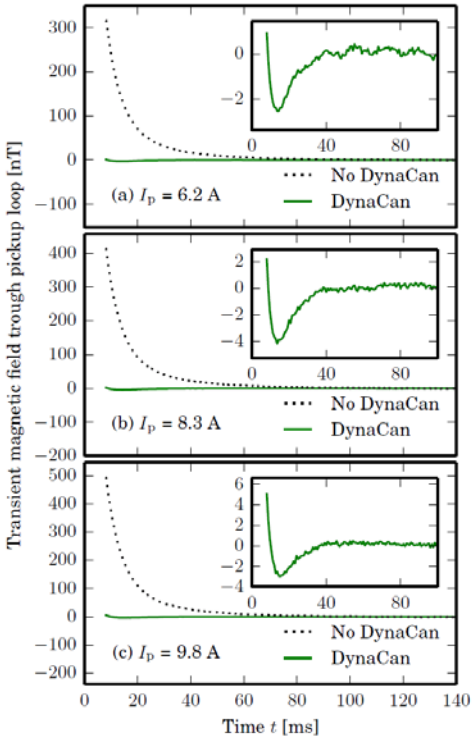

Fig. 7. Magnetic-field transients at the center of the room without (black dashed line) and with DynaCan (green solid line, also in insets) for three different B_p currents I_p: (a) 6.2 A, (b) 8.3 A, and (c) 9.8 A. Oscillations in the inset to (a) are residual 60 Hz interference.

Although the shielded room may provide a magnetically quiet environment for LF-MRI system, it makes the system immobile and increases its cost. An unshielded, portable and inexpensive LF-MRI system is attractive for, e.g., routine examination in underdeveloped countries, and remote sites. We began building unshielded systems in an urban laboratory environment in 2008 [71]. A 7-channel unshielded system was implemented by Espy *et al.* in 2015 [72].

Magnetic field fluctuations in an unshielded urban laboratory can reach hundreds of nT per minute during noisy daytime, but usually drop down to only a few nT at night. The field fluctuation causes the signal Larmor frequency to drift randomly for several Hz during the unshielded LF-NMR/MRI measurements, thus seriously spoiling the averaging effect and causing imaging artifacts [73]. An effective active compensation technique was developed, based on spatial correlation of the low-frequency magnetic field fluctuation to stabilize the B_0 field [74]. A full-tensor environmental gradient field compensation was suggested for cancelling the spatial gradients from the environment [75]. With these noise suppression techniques, a four-channel LF-MRI system for parallel imaging [76] achieved a spatial resolution better than 2.5 mm × 2.5 mm × 5 mm in vegetable imaging (**Fig. 8**).

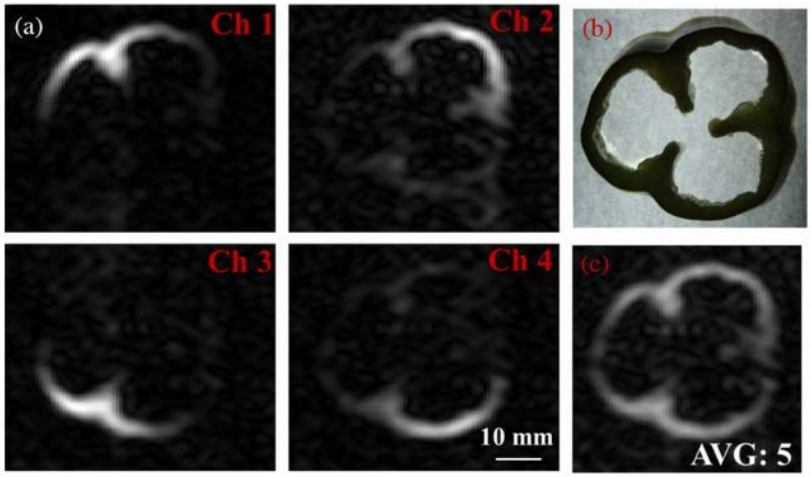

Fig. 8. (a) Two-dimensional MR images of pepper sample for each channel of the low-T_c SQUID-based second-order gradiometer system, (b) photograph of the pepper slice, (c) reconstructed MR image from the four images of (a) using the weighted superposition method. The average number of times was 5.

SQUID-based LF-MRI has been demonstrated to have many advantages [77], such as:

(1) No superconducting magnet is needed because B_0 is very low. This greatly reduces system complexity and cost, so it is possible to easily develop an open and mobile low-cost medical system.

(2) The enhanced intrinsic longitudinal relaxation times (T_1) of different soft tissues at low field can be used to distinguish cancerous and normal tissues, e.g. prostate cancer, breast cancer etc., which have poor specificities in high-field MRI [78,79,80].

(3) High-field MRI images cannot be acquired if the patient has a pacemaker, screws or other metallic implants in the body, because the susceptibility difference between metal and tissue may lead to a local field inhomogeneity proportional to B_0 strength and gives rise to image distortion. By lowering the B_0 field to microtesla range, this effect becomes negligible [81]. In addition, these objects are exposed to strong magnetic forces that might hurt the patient.

(4) Hybrid imaging by combing MEG with LF-MRI may provide functional and anatomical information of brain simultaneously, see the following section 5.

(5) The relaxation dispersion behavior reflects the B_0 field dependence of the relaxation times (typically T_1). Because of technical constraints in commercial machines, the frequency range of traditional relaxation dispersion curves obtained by fast field cycling technique usually starts from 10 kHz (234 μT) to several MHz [82]. Therefore, people developed the spin-locking technique to measure the $T_{1\rho}$ relaxation dispersion in the rotating frame at low spin-lock field to gain useful information on the composition of macromolecules, like proton exchange between water and macromolecules [83]. However, the heat produced by the spin-lock pulse usually makes the $T_{1\rho}$ technique prohibitive for human study. The LF-MRI technique enables direct T_1 and T_2 dispersion measurement at all frequencies below 10 kHz without heating problem. Inglis *et al.* showed *in vivo* human brain images at LF with distinguishable components, like brain tissue, scalp, blood and cerebrospinal fluid [84]. In order to determine whether LF-MRI has further potential advantages for *in vivo* human brain imaging, a quantitative comparison was made between relaxation dispersion in postmortem pig brain measured at ultra-low fields and spin-locking at 7 Tesla [85]. It was found that LF-MRI may offer distinct, quantitative advantages for human brain imaging, while simultaneously avoiding the severe heating limitation imposed on high-field spin-locking.

5 Hybrid biomagnetism and magnetic resonance imaging

The temporal resolution of MEG, typically 1 ms, is much better than fMRI, but a drawback of magnetic neuroimaging is the fact that the three-dimensional inverse problem is ill-posed. Helmholtz showed more than 150 years ago that it is impossible to uniquely determine the current distribution inside a conductor from a measurement of the magnetic field in its surroundings. Therefore, MEG is not perfect with respect to localization accuracy of the source. If, however, a priori information on the shape and on the conductivity of the conductor is available, the ill-posedness of the problem can be overcome. If MRI and MEG measurements are performed in different systems, data migration from one system to the other is a big challenge. In

addition, geometrical positioning errors cannot be avoided. Typically, MEG/MRI co-registration errors may reach the order of 5–10 mm in the cortex. The spatial resolution is less precise for sources in the deep brain region. Since MRI and MEG signals can be distinctly separated in the frequency domain, co-registration of both modalities is feasible. Because of simultaneous measurement, positioning errors are completely avoided. Furthermore, the combination of MEG with LF-MRI no longer requires moving the patient and reduces the total system cost. Several groups combined LF-MRI with MEG.

The Los Alamos group first demonstrated the possibility of simultaneous measurement of MEG and MRI using their homemade seven-channel low-T_c SQUID system [86]. It allows three-dimensional matching of LF-MRI images and MEG data with better accuracy than that of traditional subsequent MEG and MRI registration. They also suggested that parallel imaging of LF-MRI with hundreds of SQUID channels would significantly reduce the system noise. The total imaging time would be accelerated, which finally would make the hybrid MEG/MRI system more reliable and efficient for clinical diagnosis [87]. Subsequently, the Finnish group developed a combined MEG/MRI using a commercial whole-head 306-channel MEG machine [88]. Great efforts are made to optimize the sensors, the pulse sequences and the reconstruction methods.

6 Magnetic resonance imaging of neural activity

The magnetic field generated by neuronal activity adds to the magnetic field imposed on the human body for MR imaging. In case of LF-MRI, this local distortion of the imaging field on the order of hundreds of picotesla may affect spin dynamics because it slightly changes the imaging field in the microtesla range. This local field change may lead to a detectable change in the NMR signal. This modality is called direct neuronal imaging (DNI) [89] or neuronal current imaging (NCI) [90]. Sustained neuronal activity characterized by a local quasi-static magnetic field change can be observed as a change of the local spin-precession frequency. Fast neuronal activity may act as a tipping pulse, the so-called AC or resonant effect in NCI [91].

Using a priori information on anatomical structure and on the electrical conductivity of the different tissues in the brain may considerably improve the accuracy of source localization. MRI allows to measure the electric current density in an object by observing how the associated magnetic field affects the spin precession. This so-called current-density imaging (CDI) modality has been shown to be feasible with externally impressed current [92]. It has been shown that conductivity imaging can be done in a standard MRI system without applying a current just by post-processing analysis of the phase distribution of the imaging rf pulse [93]. Evaluation of the magnitude allows to perform permittivity imaging [94]. However, conductivity imaging is usually done in standard high-field MRI systems, leading to a measurement

of the electrical properties in the upper MHz range [95], whereas for MEG inversion, a knowledge of these quantities at sub-kHz frequencies is needed. For CDI of static currents, rotation of the object is usually needed because CDI measures only the change of the MRI main field component. The magnetization is rotated adiabatically, thus overcoming the requirement for object rotation [96]. A zero-field encoding protocol was recently published which allows to perform static CDI measurements without applying any MRI fields [97]. The obtained distribution map of conductivity and permittivity of the brain does already yield information on possible pathogenic tissue. If the knowledge of the cortical anatomy obtained with MRI and the conductivity distribution from CDI is put in to the calculation of the sources of neural signals from the field, the ill-posed inverse problem is expected to become uniquely solvable.

7 Magnetic immunoassays

Magnetic nanoparticles (MNP) are becoming increasingly popular for manipulation and examination of biological samples. MNP consisting of Magnetite (Fe_3O_4) or Maghemite (Fe_2O_3) are particularly favorable because of their biocompatibility. MNP are usually superparamagnetic, i.e. their magnetism is vanishing if no external magnetic field is present. Often, they are coated with a biocompatible surfactant, e.g. dextran or streptavidin. They can be used for sample preparation, e.g. for nucleic acid filtration [98] because they can be moved in a magnetic gradient field and thus be used for extraction and sorting. In addition, their magnetic field can be detected by a sensitive magnetometer. Thus, MNP are particularly attractive in biochemistry because they can be used both as a handle and as a marker. Albeit biomagnetic sensing using MNP markers is not a label-free technique, magnetic immunoassays are briefly covered in this chapter because the method is versatile and sensitive.

Immunoassays employ the highly specific interaction between antigenes and antibodies in conjunction with labels or markers for the detection and quantification of specific biomolecules. Typically, fluorophores, enzymes, or radioactive compounds are used as labels. However, the detection range of fluorescence markers is restricted, the sensitivity of enzyme techniques is limited and radioactive markers pose radiation hazards. Magnetic bioassays have therefore been identified as a very promising alternative [99,100].

For measuring the magnetic response of MNP with respect to a magnetic excitation field, three magnetic detection techniques are employed:

(1) Susceptometry [101] involves lock-in detection of the response to a magnetic excitation at a frequency f_0. In case of monodispersed particles, their concentration in a test volume can be quantitatively determined. In addition, the hydrodynamic size parameters of MNP can be determined [102]. If the particle sizes follow a lognormal distribution, the mean hydrodynamic radius and its standard deviation

can be determined from the measured complex magnetic susceptibility [103]. Therefore, the size enhancement due to biocompatible surface coating and subsequent functionalization and analyte binding can be measured [104]. A key disadvantage of the susceptometry technique is its lack of selectivity. In case of low concentrations of biomolecules and consequently low concentrations of magnetic marker particles, the resultant susceptibility of the solution is hard to discern from the parasitic susceptibility of the sample container, of the reagents and of the laboratory environment.

(2) Relaxometry [105] is based on recording the time transient of the magnetic response of the particles during the off-time of a pulsed excitation field. By analyzing the relaxation time of the particle's magnetization, a distinction between the Néel relaxation of bound particles and the Brownian relaxation of unbound carriers is feasible [106], since the reorientation of the magnetization vector inside the magnetic core is significantly slower than the Brownian relaxation of particles in solution. It is possible to obtain information on the size distribution of the magnetic cores of nanoparticles, especially on the mean value and the standard deviation of the core diameter of the magnetic crystallites. The technique allows to monitor binding kinetics [107]. Since the relaxometric magnetic field signals are typically very small, the technique usually requires the use of ultra-sensitive SQUIDs as magnetic field sensors. On samples with higher particle concentration, relaxometry can also be measured with fluxgate sensors [108].

(3) The frequency mixing technique [109] probes the nonlinear magnetization curve of superparamagnets. Upon magnetic excitation at two distinct frequencies f_1 and f_2 incident on the sample, the response signal generated at a frequency representing a linear combination $m \cdot f_1 + n \cdot f_2$ is detected. The appearance of these components is highly specific to the nonlinearity of the magnetization curve of the particles. With this magnetic measurement technique, a magnetic immunoassay for detection of tetanus toxoid was developed. Coaxial coils provided magnetic excitation fields at two distinct frequencies $f_1 = 49.38$ kHz and $f_2 = 61$ Hz incident on the sample. By means of a differential pickup coil, the response signal of the sample inside the coil at a frequency $f_1 + 2 \cdot f_2$ was detected. This mixing component was chosen since it is maximum for vanishing static offset field. Prior to the measurement, primary antibodies were immobilized on a polyethylene filter (Abicap from Senova, Weimar). Then, 500 µl sample was added. When the sample passed the filter, 500 µl of secondary antibody solution (anti-h-IgG biotinylated in PBS) and 500 µl magnetic bead solution (fluidMAG-Streptavidin 200 nm from chemicell, Berlin) were added and rinsed with 750 µl PBS. **Fig. 9** shows the measured signals of different tetanus immunoassay samples as a function of the concentration of the analyte. At low concentrations of the analyte, unspecific binding of MNP and the thermal noise of the detection coil determines the detection limit. At high concentrations, saturation occurs because nearly all available binding sites in the filter are occupied. Numerous magnetic immunoassays have been demonstrated [110,111, 112] which usually yielded a better sensitivity than conventional immunoassays.

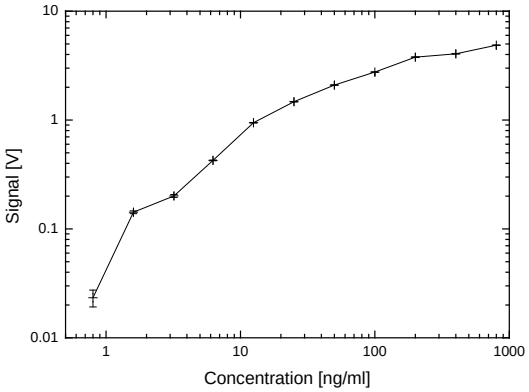

Fig. 9. Calibration curve of a magnetic tetanus immunoassay.

8 Conclusion and perspectives

Biomagnetic measurements of the magnetic field surrounding the human body, generated by the electrophysiological processes of life in the body, have developed continuously over the past decades. The evolution of supersensitive SQUID technology has led to the development of multichannel systems with hundreds of sensor channels for recording MCG and MEG. They provide unique images of heart and brain activity on a millisecond time scale. Increasing computational power and the fusion of data obtained with different imaging modalities has led to unique solutions of the inverse problem of electromagnetism and thus opened up a new window into the human body. Numerous clinical diagnostic applications of MCG, MEG and LF-MRI have been already demonstrated. LF-MRI allows more broadly applicable, less dangerous and eventually cheaper instrumentation than its well-established high field counterpart. In addition, promising first results with respect to distinction between malignant and healthy tissue have been obtained. The fusion of these techniques, in conjunction with the novel imaging modalities NCI and CDI, is expected to lead to added diagnostic value as compared to the sum of the individual techniques. Major obstacles are the need for heavy magnetic shielding and for liquid helium coolant, both of which account for a major fraction of the cost of procurement and operation. Recently, flexible shielding solutions adapted to the specific requirements of the location are being offered at affordable cost. As high-T_c SQUIDs are becoming increasingly sensitive and reliable, they might establish as an alternative in MCG instrumentation where sensitivity is not as critical as for MEG. Due to its noninvasive and almost passive nature, biomagnetic sensing is expected to become increasingly important in the near future, both in scientific research and in clinical diagnostics.

References

[1] Clarke J, Braginski, AI (eds) (2004) The SQUID Handbook, Vol. I Fundamentals and Technology of SQUIDs and SQUID Systems, Wiley-VCH, Weinheim

[2] Andrä W, Nowak H (eds) (2007) Magnetism in Medicine, 2nd Ed. Wiley-VCH, Weinheim

[3] Malmivuo J, Plonsey R (1995) Bioelectromagnetism, Principles and Applications of Bioelectric and Biomagnetic Fields. Oxford University Press, New York

[4] Erné SN, Lehmann J (1996) Magnetocardiography, an introduction. In: Weinstock H (ed) SQUID sensors: Fundamentals, Fabrication and Applications, Kluwer, Dordrecht, p 395–412

[5] Einthoven W (1902) Galvanometrische registratie van het menschelijk electrocardiogram. In: Herinneringsbudendedl Professor S.S. Rosenstein. Eduard Ijdo, Leiden: p 101–1077

[6] Baule GM, McFee R (1963) Detection of the magnetic field of the heart. Am Heart J 55:95–96

[7] Jaklevic RC, Lambe J, Silver AH, Mercereau JE (1964) Quantum interference effects in Josephson tunneling. Phys Rev Lett 12:159–160

[8] Zimmerman JE, Thiene P, Harding JT (1970) Design and operation of stable rf-biased superconducting point-contact quantum devices, and a note on the properties of perfectly clean metal contacts. J Appl Phys 41:1572–80

[9] Cohen D, Edelsack EA, Zimmerman JE (1970) Magnetocardiograms taken inside a shielded room with a superconducting point-contact magnetometer. Appl Phys Lett 16:278–280

[10] Nowak H (2015) SQUIDs in Biomagnetism. In: Seidel P (ed) Applied Superconductivity, Wiley-VCH, Weinheim

[11] Stroink G, Hailer B, van Leeuwen P (2007) Cardiomagnetism. In: Andrä W, Nowak H (eds) Magnetism in Medicine, 2nd Ed. Wiley-VCH, Weinheim, p 164–209

[12] Fenici R, Brisinda D, Sorbo AR, Venuti A (2012) MCG Instrumentation and Application. In: Rogalla H, Kes PH (eds) 100 Years of Superconductivity, CRC Press, Boca Raton, p 582–602

[13] Ilmoniemi RJ, Hari R, Reinikainen K (1984) A four-channel SQUID magnetometer for brain research. Electroenceph Clin Neurophysiol 58:467–473

[14] Nowak H (2007) Biomagnetic Instrumentation. In: Andrä W, Nowak H (eds) Magnetism in Medicine, 2nd Ed. Wiley-VCH, Weinheim, p 101–163

[15] Saarinen M, Karp PJ, Katila, TE, Siltanen P (1974) The magnetocardiogram in cardiac disorders. Cardiovascular Res 8:820–834

[16] Dilorio MS, Yang KY, Yoshizumi S (1995) Biomagnetic measurements using low-noise integrated SQUID magnetometers operating in liquid nitrogen. Appl Phys Lett 67:1926–1928

[17] Itozaki H, Tanaka S, Toyoda H, Hirano T, Haruta Y, Nomura M, Saijou T, Kado H (1996) A multi-channel high-T_c SQUID system and its applications. Supercond Sci Technol 9:A38–A41

[18] David B, Grundler D, Krey S, Doormann V, Eckard R, Krumme JP, Rabe G, Dössel O (1996) High-T_c-SQUID magnetometers for biomagnetic measurements. Supercond Sci Technol 9:A96–A99
[19] Zhang Y, Wolters N, Schubert J, Lomparski D, Banzet M, Panaitov G, Krause HJ, Mück M, Braginski AI (2003) HTS SQUID gradiometer using substrate resonators operating in unshielded environment – a portable MCG system. IEEE Trans Appl Supercond 13:389–392
[20] Zhang Y, Wolters N, Lomparski D, Zander W, Banzet M, Schubert J, Krause HJ, van Leeuwen P (2005) Multi-channel HTS rf SQUID gradiometer system recording fetal and adult magnetocardiograms. IEEE Trans Appl Supercond 15:631–634
[21] Tolstrup K, Madsen BE, Ruiz JA, Greenwood SD, Camacho J, Siegel RJ, Gertzen HC, Park JW, Smars PA (2006) Non-invasive resting magnetocardiographic imaging for the rapid detection of ischemia in subjects presenting with chest pain. Cardiology 106:270–276
[22] Morguet AJ, Behrens S, Kosch O, Lange C, Zabel M, Selbig D, Munz DL, Schultheiss HP, Koch H (2004) Myocardial viability evaluation using magnetocardiography in patients with coronary artery disease. Coron Artery Dis 15:155–62
[23] Park JW, Leithäuser B, Vrsansky M, Jung F (2008) Dobutamine stress magnetocardiography for the detection of significant coronary artery stenoses – A prospective study in comparison with simultaneous 12-lead electrocardiography. Clin Hemorheol Microcirc 39:21–32
[24] Kwong JSW, Leithäuser B, Park JW, Yu CM (2013) Diagnostic value of magnetocardiography in coronary artery disease and cardiac arrhythmias: A review of clinical data. Int J Cardiol 167:1835–1842
[25] Shin ES, Lam YY, Her AY, Brachmann J, Jung F, Park JW (2017) Incremental diagnostic value of combined quantitative and qualitative parameters of magnetocardiography to detect coronary artery disease. Int J Cardiol 228:948–952
[26] Fenici RR, Masselli M, Lopez L, Sabetta F (1985) High resolution magnetocardiography: electrophysiological and clinical findings. Med Biol Eng Comput 23:1475–1478
[27] Brisinda D, Fenici R (2007) Noninvasive classification of ventricular preexcitation with unshielded magnetocardiography and transesophageal atrial pacing and follow-up. Pacing Clin Electrophysiol 30 (Suppl 1):S151-S155
[28] Kariniemi V, Ahopelto J, Karp PJ, Katila TE (1974) The fetal magnetocardiogram. J Perinat Med 2:214-216
[29] Schneider U, Schleussner E (2007) Fetal Magnetography. In: Andrä W, Nowak H (eds) Magnetism in Medicine, 2nd Ed. Wiley-VCH, Weinheim, p 268–290
[30] Stinstra J, Golbach E, van Leeuwen P, Lange S, Menendez T, Moshage W, Schleussner E, Kaehler C, Horigome H, Shigemitsu S, Peters MJ (2002) Multicentre study of fetal cardiac time intervals using magnetocardiography. Br J Obstet Gynaecol 109:1235-1243

[31] van Leeuwen P, Hailer P, Bader W, Geissler J, Trowitsch E, Grönemeyer D (1999) Magnetocardiography in the diagnosis of fetal arrhythmia. Br J Obstet Gynaecol 106:1200-1208
[32] Srinivasan S, Strasburger J (2008) Overview of fetal arrythmias. Curr Opin Pediatr 20:522–531
[33] Zhang Y, Wolters N, Lomparski D, Zander W, Banzet M, Schubert J, Krause HJ, Geue D, van Leeuwen P (2006) Foetal magnetocardiography with a multichannel HTS rf SQUID gradiometer. Supercond Sci Technol 19:S266–S270
[34] Knösche TR, Nakasato N, Eiselt M, Haueisen J (2007) Neuromagnetism. In: Andrä W, Nowak H (eds) Magnetism in Medicine, 2nd Ed. Wiley-VCH, Weinheim, p 210–267
[35] Del Gratta C, Della Penna S, Pizzella V, Romani GL (2012) Medical Applications of Magnetoencephalography. In: Rogalla H, Kes PH (eds) 100 Years of Superconductivity, CRC Press, Boca Raton, p 562–581
[36] Gross J, Ioannides AA, Dammers J, Maess B, Friederici AD, Mollergartner HJ (1998) Magnetic field tomography analysis of continuous speech. Brain Topogr 10:273–281
[37] Kutas M, Hillyard SA (1980) Reading senseless sentences: Brain potentials reflecting semantic incongruity. Science 207:203–205
[38] Kober H, Moller M, Nimsky C, Vieth J, Fahlbusch R, Ganslandt O (2001) New approach to localize speech relevant brain areas and hemispheric dominance using spatially filtered magnetoencephalography. Hum Brain Mapp 14:236–250
[39] Halgren E, Dhond RP, Christensen N, van Petten C, Marinkovic K, Lewine JD, Dale AM (2002) N400-like magnetoencephalography responses modulated by semantic context, word frequency, and lexical class in sentences. NeuroImage 17:1101–1116
[40] Neuhaus C, Knösche TR, Friederici AD (2006) Effects of musical expertise and boundary markers on phrase perception in music. J Cogn Neurosci 18:472–493
[41] Kuriki S, Isahai N, Ohtsuka A (2005) Spatiotemporal characteristics of the neural activities processing consonant/dissonant tones in melody. Exp Brain Res 162:46–55
[42] Herrmann CS, Munk MHJ, Engel AK (2004) Cognitive functions of gamma band activity: memory match and utilization. Trends Cogn Sci 8:347–355
[43] Okusa T, Kakigi R, Osaka N (2000) Cortical activity related to cue-invariant shape perception in humans. Neuroscience 98:615–624
[44] Feige B, Kristeva-Feige R, Rossi S, Pizzella V, Rossini PM (1996) Neuromagnetic study of movement-related changes in rhythmic brain activity. Brain Res 734:252–260
[45] Nakasato N, Yoshimoro T (2000) Somatosensory, auditory and visual evoked magnetic fields in patients with brain diseases. J Clin Neurophysiol 17:201–211
[46] Knowlton RC, Shih J (2004) Magnetoencephalography in epilepsy. Epilepsia 45:61–71

[47] Vieth J., Kober H, Weise E, Daun A, Moeger A, Friedrich S, Pongratz H (1992) Functional 3D localization of cerebrovascular accidents by magneto-encephalography (MEG). Neurol Res 14:132–134
[48] Qiao F, Kuroda S, Kamada K, Houkin K, Iwasaki Y (2003) Source local-ization of the re-build up phenomenon in pediatric moyamoya disease – a dipole distribution analysis using MEG and SPECT. Childs Nem Syst 19:760–764
[49] Seki S, Nakasato N, Ohtomo S, Kanno A, Shimizu H, Tominaga T (2005) Neuromagnetic measurement of unilateral temporo-parietal theta rhythm in patients with internal carotid artery occlusive disease. NeuroImage 25:502–510
[50] Dammers J, Chocholacs H, Eich E, Boers F, Faley MI, Dunin-Borkowski RE, Shah NJ (2014) Source localization of brain activity using helium-free interferometer. Appl Phys Lett 104:213705
[51] Callaghan PT (1991) Principles of Nuclear Magnetic Resonance Microscopy. Clarendon Press, Oxford
[52] Haacke EM, Brown RW, Thompson MR, Venkatesan R (1999) Magnetic Resonance Imaging Physical Principles and Sequence Design. Wiley-Liss, New York
[53] Abragam A (1961) The Principle of Nuclear Magnetism. Oxford University Press, London
[54] Purcell EM, Torrey H, Pound RV (1946) Resonance absorption by nuclear magnetic moments in a solid. Phys Rev 69:37–38
[55] Bloch F, Hansen WW, Packard M (1946) Nuclear Induction. Phys Rev 69:127
[56] Ernst RR, Anderson WA (1966) Application of Fourier transform spectroscopy to magnetic resonance. Rev Sci Instrum 37:93–102
[57] Lauterbur PC (1973) Image formation by induced local interactions: examples employing nuclear magnetic resonance. Nature 242:190–191
[58] Mansfield P (1977) Multi-planar image formation using NMR spin echoes. J Phys C 10:L55–L58
[59] Huettel SA, Song AW, McCarthy G (2009) Functional Magnetic Resonance Imaging, 2nd Ed. Sinauer Associates, Sunderland, MA
[60] Li X (2014) Functional Magnetic Resonance Imaging Processing. Springer, Dordrecht
[61] Dumoulin CL, Souza SP, Walker MF, Wagle W (1989) Three-dimensional phase contrast angiography. Magn Reson Med 9:139–149
[62] Nishimura DG (1990) Time-of-flight MR angiography. Magn Reson Med 14:194–201
[63] Koh DM, Collins DJ (2007) Diffusion-weighted MRI in the body: applications and challenges in oncology. Am J Roentgenol 188:1622-1635
[64] Le Bihan D, Mangin JF, Poupon C, Clark CA, Pappata S, Molko N, Chabriat H (2001) Diffusion tensor imaging: concepts and applications. J Magn Reson Imaging 13: 534-546
[65] Matson GB, Weiner MW (1992) Spectroscopy. In: Stark DD, Bradley WG (eds) Magnetic Resonance Imaging. Mosby Yearbook, St. Louis, p 438–477
[66] Konstandin S, Schad LR (2014) 30 years of sodium/X-nuclei magnetic resonance imaging. Magn Reson Mater Phys 27:1–4

[67] Ogawa S, Tank DW, Menon R, Ellermann JM, Kim SG, Merkle H, Ugurbil K (1992) Intrinsic signal changes accompanying sensory stimulation: functional brain mapping with magnetic resonance imaging. Proc Natl Acad Sci USA 89:5951–5955

[68] Lee JH, Durand R, Gradinaru V, Zhang F, Goshen I, Kim DS, Fenno LE, Ramakrishnan C, Deisseroth K (2010) Global and local fMRI signals driven by neurons defined optogenetically by type and wiring. Nature 465:788–792

[69] Clarke J (2011) Ultralow field NMR and MRI. In: Rogalla H, Kes PH (eds) 100 Years of Superconductivity, CRC Press, Boca Raton, p 610–619

[70] Zevenhoven KCJ, Dong H, Ilmoniemi RJ, Clarke J (2015) Dynamical cancellation of pulse-induced transients in a metallic shielded room for ultra-low-field magnetic resonance imaging. Appl Phys Lett 106:034101

[71] Dong H, Wang Y, Zhang L, Sun Y, Xie X (2008) Detection of proton NMR signal in the earth's magnetic field at an urban laboratory environment without shielding. Supercond Sci Technol 20:115009

[72] Espy MA, Magnelind PE, Matlashov AN, Newman SG, Sandin HJ, Schultz LJ, Sedillo R, Urbaitis AV, Volegov PL (2015) Progress toward a deployable SQUID-based ultra-low field MRI system for anatomical imaging. IEEE Trans Appl Supercond 25:1601705

[73] Liu C, Chang B, Qiu L, Dong H, Qiu Y, Zhang Y, Krause HJ, Offenhäusser A, Xie X (2015) Effect of magnetic field fluctuation on ultra-low field MRI measurements in the unshielded laboratory environment. J Magn Reson 257:8–14

[74] Qiu L, Liu C, Dong H, Xu L, Zhang Y, Krause HJ, Xie X (2012) Magnetic field improved ULF-NMR measurement in an unshielded laboratory using a low-Tc SQUID. Physics Procedia 36:388–93.

[75] Dong H, Qiu L, Shi W, Chang B, Qiu Y, Xu L, Liu C, Zhang Y, Krause HJ, Offenhäusser A, Xie X (2013) Ultra-low field magnetic resonance imaging detection with gradient tensor compensation in urban unshielded environment. Appl Phys Lett 102:102602

[76] Liu C, Chang B, Qiu L, Qiu Y, Dong H, Zhang Y, Xie X (2015) Multichannel ULF-MRI study in magnetic unshielded urban laboratory environment. IEEE Trans Appl Supercond 25:1602804

[77] Clarke J, Hatridge M, Mößle M (2007) SQUID-detected magnetic resonance imaging in microtesla fields. Annu Rev Biomed Eng 9:389–413

[78] Lee SK, Mößle M, Myers W, Kelso N, Trabesinger AH, Pines A, Clarke J (2005) SQUID-detected MRI at 132 μT with T_1-weighted contrast established at 10 μT-300 mT. Magn Reson Med 53:9–15

[79] Busch S, Hatridge M, Mößle M, Myers W, Wong T, Mück M, Chew K, Kuchinsky K, Simko J, Clarke J (2012) Measurements of T_1-relaxation in ex vivo prostate tissue at 132 μT. Magn Reson Med 67:1138–1145

[80] Lee SJ, Shim JH, Kim K, Hwang S, Yu KK, Lim S, Han JH, Yim H, Kim JH, Jung YS, Kim KS (2015) T_1 relaxation measurement of ex-vivo breast cancer tissues at ultralow magnetic fields. BioMed Res Int 2015:385428

[81] Mößle M, Han SI, Myers WR, Lee SK, Kelso N, Hatridge M, Pines A, Clarke J (2006) SQUID-detected microtesla MRI in the presence of metal. J Magn Reson 179:146–151
[82] Kimmich R, Anoardo E (2004) Field cycling NMR relaxometry. Prog Nucl Magn Reson 44:257–320
[83] Gilani IA, Sepponen R (2016) Quantitative rotating frame relaxometry methods in MRI. NMR Biomed 29:841–861
[84] Inglis B, Buckenmaier K, SanGiorgio P. Pedersen AF, Nicols MA, Clarke J (2013) MRI of the human brain at 130 microtesla. Proc Natl Acad Sci USA 110:19194–19201
[85] Dong H, Hwang Sm, Wendland M, You L, Clarke J, Inglis B (2017) Ultralow-field and spin-locking relaxation dispersion in post mortem pig brain. Magn Reson Med, DOI: 10.1002/mrm.26621
[86] Zotev VS, Matlashov AN, Volegov PL, Savukov IM, Espy MA, Mosher JC, Gomez JJ, Kraus Jr RH (2008) Microtesla MRI of the human brain combined with MEG. J Magn Reson 194:115–20
[87] Matlashov AN, Burmistrov E, Magnelind PE, Schultz L, Urbaitis AV, Volegov PL, Yoder J, Espy MA (2012) SQUID-based systems for co-registration of ultra-low field nuclear magnetic resonance images and magnetoencephalography. Physica C 482:19–26
[88] Vesanen PT, Nieminen JO, Zevenhoven KCJ, Dabek J, Parkkonen LT, Zhdanov AV, Luomahaara J, Hassel J, Penttilä J, Simola J, Ahonen AI, Mäkelä JP, Ilmoniemi RJ (2013) Hybrid ultra-low-field MRI and magnetoencephalography system based on a commercial whole-head neuromagnetometer. Magn Reson Med 69:1795–1804
[89] Bodurka J, Bandettini PA (2002) Toward direct mapping of neuronal activity: MRI detection of ultraweak, transient magnetic field changes. Magn Reson Med 47:1052–8
[90] Burghoff M, Albrecht HH, Hartwig S, Hilschenz I, Körber R, Höfner N, Scheer HJ, Voigt J, Trahms L, Curio G (2010) On the feasibility of neurocurrent imaging by low field nuclear magnetic resonance. Appl Phys Lett 96:233701
[91] Körber R, Nieminen JO, Höfner N, Jazbinsek V, Scheer HJ, Kim K, Burghoff M (2013) An advanced phantom study assessing the feasibility of neuronal current imaging by ultra-low field NMR. J Magn Reson 237:182–190
[92] Oh SH, Lee BI, Woo EJ, Lee SY, Cho MH, Kwon O, Seo JK (2003) Conductivity and current density image reconstruction using harmonic B_z algorithm in magnetic resonance electrical impedance tomography. Phys Med Biol 48:3101–16
[93] Voigt T, Katscher U, Doessel O (2011) Quantitative conductivity and permittivity imaging of the human brain using electric properties tomography. Magn Reson Med 66:456–66
[94] Kim DH, Choi N, Gho SM, Shin J, Liu C (2014) Simultaneous imaging of in vivo conductivity and susceptibility. Magn Reson Med 71:1144–1150
[95] Woo EJ, Seo JK (2008) Magnetic resonance electrical impedance tomography (MREIT) for high-resolution conductivity imaging. Physiol Meas 29:R1-26

[96] Nieminen JO, Zevenhoven KCJ, Vesanen P, Hsu YC, Ilmoniemi RJ (2014) Current-density imaging using ultra-low-field MRI with adiabatic pulses. Magn Reson Imaging 32:54–59

[97] Vesanen P, Nieminen JO, Zevenhoven KCJ, Hsu YC, Ilmoniemi RJ (2014) Current-density imaging using ultra-low-field MRI with zero-field encoding. Magn Reson Imaging 32:766–770

[98] Häfeli U, Schütt W, Teller J, Zborowski M (eds.) (1997) Scientific and Clinical Applications of Magnetic Carriers, Plenum, N.Y.

[99] Thanh NTK (ed.) (2012) Magnetic Nanoparticles - From Fabrication to Clinical Applications, CRC Press, Taylor & Francis Group, Boca Raton

[100] Cardoso S, Leitao DC, Dias TM, Valadeiro J, Silva MD, Chicharo A, Silverio V, Gaspar J, Freitas PP (2017) Challenges and trends in magnetic sensor integration with microfluidics for biomedical applications. J Phys D 50:213001

[101] Kriz K, Gehrke J, Kriz D (1998) Advancements toward magneto immunoassays. Biosens Bioelectron 13:817–823

[102] Payet B, Vincent D, Delaunay L, Noyel G (1998) Influence of particle size distribution on the initial susceptibility of magnetic fluids in the Brown relaxation range. J Magn Magn Mater 186:168–174

[103] Ludwig F, Heim E, Schilling M (2009) Characterization of magnetic core-shell nanoparticles by fluxgate magnetorelaxometry, ac susceptibility, transmission electron microscopy and photon correlation spectroscopy–a comparative study. J Magn Magn Mater 321:1644–1647

[104] Prieto Astalan A, Jonasson C, Petersson K, Blomgren J, Ilver D, Krozer A, Johansson C (2007) Magnetic response of thermally blocked magnetic nanoparticles in a pulsed magnetic field. J Magn Magn Mater 311:166–170

[105] Matz H, Drung D, Hartwig S, Gross H, Kötitz R, Müller W, Vass A, Weitschies W, Trahms L (1998) A SQUID measurement system for immunoassays. Appl Supercond 6:577–583

[106] Kötitz R, Fannin PC, Trahms L (1995) Magnetorelaxometry domain study of Brownian and Néel relaxation in ferrofluids. J Magn Magn Mater 149:42–46

[107] Eberbeck D, Wiekhorst F, Steinhoff U, Schwarz KO, Kummrow A, Kammel M, Neukammer N, Trahms L (2009) Specific binding of magnetic nanoparticle probes to platelets in whole blood detected by magnetorelaxometry. J Magn Magn Mater 321:1617–1620

[108] Ludwig F, Heim E, Schilling M (2007) Characterization of superparamagnetic nanoparticles by analyzing the magnetization and relaxation dynamics using fluxgate magnetometers. J Appl Phys 101:113909

[109] Krause HJ, Wolters N, Zhang Y, Offenhäusser A, Miethe P, Meyer MHF, Hartmann M, Keusgen M (2007) Magnetic particle detection by frequency mixing for immunoassay applications. J Magn Magn Mater 311:436–444

[110] Meyer MHF, Hartmann M, Krause HJ, Blankenstein G, Müller-Chorus B, Oster J, Miethe P, Keusgen M (2007) CRP determination based on a novel magnetic biosensor. Biosens Bioelectron 22:973–979

[111] Hong HB, Krause HJ, Song KB, Choi CJ, Chunga MA, Offenhäusser A (2011) Detection of two different Influenza A viruses using an ELIFA system and a magnetic biosensor. J Immunol Meth 365:95–100

[112] Rettcher S, Jungk F, Kühn C, Krause HJ, Nölke G, Commandeur U, Fischer R, Schillberg S, Schröper F (2015) A simple and portable magnetic immunoassay for the rapid detection and sensitive quantification of plant viruses. Appl Environ Microbiol 81:3039–3048